ACS APPLIED MATERIALS & INTERFACES

Research Article

www.acsami.org

Synthesis of Ultrathin Nitrogen-Doped Graphitic Carbon Nanocages as Advanced Electrode Materials for Supercapacitor

Yueming Tan,[†,‡] Chaofa Xu,[‡] Guangxu Chen,[‡] Zhaohui Liu,[‡] Ming Ma,[†] Qingji Xie,*[,†] Nanfeng Zheng,*[,‡] and Shouzhuo Yao[†]

[†]Key Laboratory of Chemical Biology and Traditional Chinese Medicine Research (Ministry of Education of China), College of Chemistry and Chemical Engineering, Hunan Normal University, Changsha 410081, China

[‡]State Key Laboratory for Physical Chemistry of Solid Surfaces and Department of Chemistry, College of Chemistry and Chemical Engineering, Xiamen University, Xiamen 361005, China

Supporting Information

ABSTRACT: Synthesis of nitrogen-doped carbons with large surface area, high conductivity, and suitable pore size distribution is highly desirable for high-performance supercapacitor applications. Here, we report a novel protocol for template synthesis of ultrathin nitrogen-doped graphitic carbon nanocages (CNCs) derived from polyaniline (PANI) and their excellent capacitive properties. The synthesis of CNCs involves one-pot hydrothermal synthesis of Mn_3O_4@PANI core−shell nanoparticles, carbonization to produce carbon coated MnO nanoparticles, and then removal of the MnO cores by acidic treatment. The CNCs prepared at an optimum carbonization temperature of 800 °C (CNCs-800) have regular frameworks, moderate graphitization, high specific surface area, good mesoporosity, and appropriate N doping. The CNCs-800 show high specific capacitance (248 F g^{-1} at 1.0 A g^{-1}), excellent rate capability (88% and 76% capacitance retention at 10 and 100 A g^{-1}, respectively), and outstanding cycling stability (~95% capacitance retention after 5000 cycles) in 6 M KOH aqueous solution. The CNCs-800 can also exhibit great pseudocapacitance in 0.5 M H_2SO_4 aqueous solution besides the large electrochemical double-layer capacitance. The excellent capacitance performance coupled with the facile synthesis of ultrathin nitrogen-doped graphitic CNCs indicates their great application potential in supercapacitors.

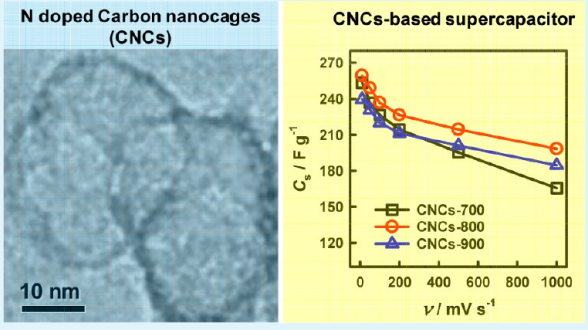

KEYWORDS: *carbon nanocage, nitrogen-doped carbon, polyaniline, pseudocapacitance, supercapacitor*

1. INTRODUCTION

The development of novel, low-cost, environmentally friendly, and high-performance energy storage systems has been under an ever increasing demand as a result of the needs of modern society and emerging ecological concerns. Supercapacitors are supposed to be a kind of promising candidate for alternative energy storage devices because of their unique advantages including high rate capability, pulse power supply, long cycle life, superior reversibility, simple principle, facile dynamics of charge propagation, and low maintenance cost.[1−6] Supercapacitors have extensive applications, including consumer electronics, energy management, memory back-up systems, industrial power, and mobile electrical systems.[7−9] The charge storage mechanism of supercapacitors is based on the interfacial double layer of electrodes with high specific surface area,[10−13] and/or based on the pseudocapacitance associated with fast surface redox reactions at some metal oxides/hydroxides, such as RuO_2,[14,15] MnO_2,[16−19] CO_3O_4,[20] and $Ni(OH)_2$,[21] conducting polymers,[22−24] and carbons rich in oxygen- and nitrogen-containing surface functional groups.[10]

Among different types of supercapacitors, electrochemical double-layer capacitors (EDLCs) using carbons as active materials are the most commonly used supercapacitors at present because of their low cost and high operational stability.[10−13] The electrode material is the key component determining the capacitance performance of EDLCs. Various carbon materials, including activated carbon,[25−30] mesoporous carbons,[31−34] carbon nanotubes (CNTs),[35−37] and graphene,[38−42] have been investigated for use as electrode materials in EDLCs. Activated carbon has been used in commercial supercapacitors because of its high specific surface area and low cost. EDLCs based on activated carbon usually have high specific capacitance at low discharging rate, but the specific capacitance decreases dramatically with increasing the discharging rate mainly because of the increasing mass-transfer resistance through the small-sized tunnels.[25−30] Mesoporous carbons of suitable pore size are more suitable for applications

Received: January 11, 2013
Accepted: February 21, 2013
Published: February 21, 2013

to high power-density EDLCs.[31−34] However, the maximum specific capacitance is still not high enough, probably due to the relatively low conductivity of porous carbon materials in most cases.[43] CNTs with high conductivity and regular structure have also been explored as electrode materials of EDLCs.[35−37] Unfortunately, CNT-based EDLCs cannot meet acceptable performance, mainly due to the relatively small specific surface area (typically <400 m^2 g^{-1}). Graphene with unique plane structure has very high conductivity and large surface area and is an ideal electrode material for EDLCs. However, the exfoliated graphene tends to restack, thus limiting its capacitance and practical applications.[44−46] To make graphene fit for EDLCs applications, many studies on efficient assembly of graphene have been conducted.[44,47,48] Despite the great efforts in synthesis of carbon-based electrode materials, the facile synthesis of carbons with large surface area, high conductivity, and suitable pore size distribution for high-performance supercapacitor applications is still of great interest and importance.

Previous studies have revealed that nitrogen functionalization of carbon materials can improve their capacitance properties,[49−60] but little nitrogen-doped carbons can serve as electrode materials for both high-capacitance and high-rate supercapacitors. Herein, we report a novel and template method to prepare ultrathin nitrogen-doped graphitic carbon nanocages (CNCs) with polyaniline (PANI) as carbon source. The CNCs prepared at a carbonization temperature of 800 °C (CNCs-800) have regular frameworks, moderate graphitization, high specific surface area, good mesoporosity, and appropriate N doping. The unique structure of CNCs-800 possesses several major advantages for supercapacitor application: (1) the ultrathin carbon shells of CNCs-800 ensure high specific surface area, which is beneficial for accumulating a large amount of charges; (2) the mesoporous structure of CNCs-800 can contribute to the enhancement of the diffusion rate of the charge carriers in the frameworks; and (3) the interconnected graphitic frameworks of CNCs-800 can ensure fast electron transfer. As a result, the CNCs-800 material show high specific capacitance, outstanding rate capability, and excellent cycling stability, which is a promising electrode material for supercapacitor.

2. EXPERIMENTAL SECTION

Instrumentation and Chemicals. Transmission electron microscopy (TEM) studies were performed on a TECNAI F-30 high-resolution transmission electron microscope operating at 300 kV. The samples were prepared by dropping ethanol dispersion of samples onto 300-mesh carbon-coated copper grids and immediately evaporating the solvent. X-ray diffraction (XRD) measurements were carried out on a PANalytical X'pert PRO diffractometer using Cu Kα radiation, operating at 40 kV and 30 mA. Thermogravimetric analysis (TGA) of samples was performed on a SDT-Q600 simultaneous TGA/DSC thermogravimetric analyzer (TA Instruments), and the samples were heated under air atmosphere from room temperature to 800 °C at 10 °C min^{-1}. X-ray photoelectron spectroscopy (XPS) was recorded on a PHI QUANTUM 2000 X-ray photoelectron spectroscopic instrument. Surface area and pore size were determined by a Surface Area and Porosity Analyzer (Micromeritics Instrument Corp. ASAP2020). All chemicals were of analytical grade and used without further purification. Ultrapure water (Millipore, ≥18 MΩ cm) was used throughout.

Synthesis of Ultrathin N-Doped Carbon Nanocages. An aqueous solution containing 0.033 M $Mn(NO_3)_2$ and 0.033 M aniline was mixed with 0.033 M $KMnO_4$ aqueous solution of equal volume under continuous stirring for about 30 min. The resulting solution was transferred into a Teflon-lined stainless steel autoclave and heated at 180 °C for 4 h, followed by natural cooling to room temperature. The precipitates were collected by centrifugation, washed with water, and finally dried at 60 °C. Then, the resulting products were carbonized into carbon-coated MnO nanoparticles under flowing argon at 700, 800, or 900 °C for 4 h. Finally, the as-prepared MnO@C nanoparticles were etched in excessive 1 M HNO_3 aqueous solution. The resulting products were collected by centrifugation, washed with water for several times, and finally dried at 60 °C.

Electrochemical Measurements. All electrochemical experiments were carried out on a CHI 760D electrochemical workstation. CNC-based supercapacitors were assembled in a symmetrical two-electrode configuration. The electrode was fabricated by pressing a mixture of 80 wt % active material, 10 wt % acetylene black, and 10 wt % polyvinylidene fluoride (PVDF) onto a piece of nickel foil (1.5 cm^2). Two electrodes were assembled with a polypropylene membrane (MPF45AC200, SCM Industrial Chemical CO.,LTD) sandwiched between them. The mass loading of active material in each electrode was 2.2 mg. The electrolytic solution was 6 M KOH. Cyclic voltammograms were obtained in the voltage range between 0 and 1 V at scan rates from 10 to 1000 mV s^{-1}. Galvanostatic charge−discharge measurements were carried out at current density from 1 to 100 A g^{-1} in the voltage range between 0 and 1 V. Electrochemical impedance spectroscopy (EIS) measurement was carried out by applying a voltage amplitude of 5 mV in the 10 kHz to 10 mHz frequency range. The specific capacitance (C_s, F g^{-1}) is calculated from the cyclic voltammograms according to the following equation:[3,10]

$$C_s = \frac{C}{m} \times 4 = \frac{Q}{U \times m} \times 4$$

where C (F) is the measured capacitance for the two-electrode cell; m (g) is the total mass of the active materials on the two electrodes; the multiplier of 4 adjusts the capacitance of the cell and the combined mass of two electrodes to the capacitance and mass of a single electrode; Q (C) is the integrated voltammetric charge; and U (V) is the voltage range of cyclic voltammogram.

The specific capacitance is also calculated from the discharge curves according to the following equation:[3,10]

$$C_s = \frac{i \times \Delta t}{\Delta V \times m} \times 4$$

where i (A) is the discharge current, Δt (s) is the discharge time, ΔV (V) is the voltage change (excluding the iR drop) within the discharge time, and m (g) is the total mass of the active materials on the two electrodes.

The energy density (E, J g^{-1}) and power density (P, W g^{-1}) derived from the charge−discharge curves are calculated by the following equations:[3,10]

$$E = \frac{C_s \times \Delta V^2}{8}$$

$$P = \frac{E}{t}$$

Electrochemical characterization of CNCs-800 in a 0.5 M H_2SO_4 aqueous solution was conducted using a three-electrode system. The working electrode was fabricated by casting Nafion-impregnated carbon ink onto a 5 mm diameter glassy carbon disk electrode. Briefly, a suspension of CNCs-800 with a concentration of 2.0 mg mL^{-1} was prepared by ultrasonically dispersing CNCs-800 (10 mg) in a mixture (5 mL) of water, ethanol, and Nafion (5 wt %) with the volume ratio of 4.0:0.8:0.2. The suspension (40 μL) was then dropped onto the glassy carbon disk and dried in air. The reference electrode and counter electrode were a saturated calomel reference electrode (SCE) and a platinum foil, respectively. All the potentials in the three-electrode system are reported with respect to SCE. The percentage of pseudocapacitance (η) is calculated from the discharge curves according to the following equation:

$$\eta = \frac{\Delta t_T - \Delta t_D}{\Delta t_T} \times 100\%$$

where Δt_D is the discharge time of the double-layer capacitance type and Δt_T is the total discharge time of the overall capacitance.

3. RESULTS AND DISCUSSION

As shown in Scheme 1, the synthesis of ultrathin nitrogen-doped graphitic CNCs involves one-pot hydrothermal synthesis of Mn_3O_4@PANI core–shell nanoparticles, followed by carbonization to yield ultrathin nitrogen-doped graphitic carbon coated MnO nanoparticles, and finally acid leaching of MnO cores. In the first step, Mn_3O_4@PANI core–shell nanoparticles were synthesized by one-pot hydrothermal treatment of a mixture containing aniline, $Mn(NO_3)_2$, and $KMnO_4$.[61] The morphologies of the prepared Mn_3O_4@PANI core–shell nanoparticles were examined by transmission electron microscopy (TEM) As shown in Figure 1a–c, the nanoparticles are coated uniformly with a thin polymer layer. The corresponding X-ray diffraction (XRD) pattern is shown in Figure S1, Supporting Information, and the peaks can be assigned to pure hausmannite Mn_3O_4 phase (JCPDS 24-0734). Then, the as-prepared Mn_3O_4@PANI nanoparticles underwent heat treatment at 800 °C under Ar atmosphere for 4 h. As shown in Figure 1d–f, a thin carbon shell can be observed on the nanoparticles. The XRD result also reveals that annealed Mn_3O_4 nanoparticles were completely converted into MnO phase (JCPDS 75-0626) in the inert atmosphere (Figure S1, Supporting Information). The curved lattice fringes in high resolution TEM (HRTEM) image clearly show graphitic (002) layers with an interplanar spacing of 0.34 nm (Figure 1f). The little distortion of circular stripes should be attributed to defects formed in the graphitization process. Graphitization occurs at such a low temperature, indicating that the manganese-oxide cores can serve as catalyst for graphitization of carbon shells.

To produce CNCs, ultrathin graphitic carbon coated MnO nanoparticles were etched in 1 M HNO_3 aqueous solution to remove the embedded MnO cores. After removing the MnO cores, utrathin CNCs (ca. 2 nm) can be observed stacking on the TEM grid and forming regular frameworks (Figure 2a–c). As shown in Figure S1, Supporting Information, a small diffraction peak at 26.0° can be attributed to the (002) plane of the hexagonal graphite structure, suggesting the presence of moderate graphitic carbon, well consistent with the HRTEM

Scheme 1. Illustration of the Synthetic Procedures of Carbon Nanocages

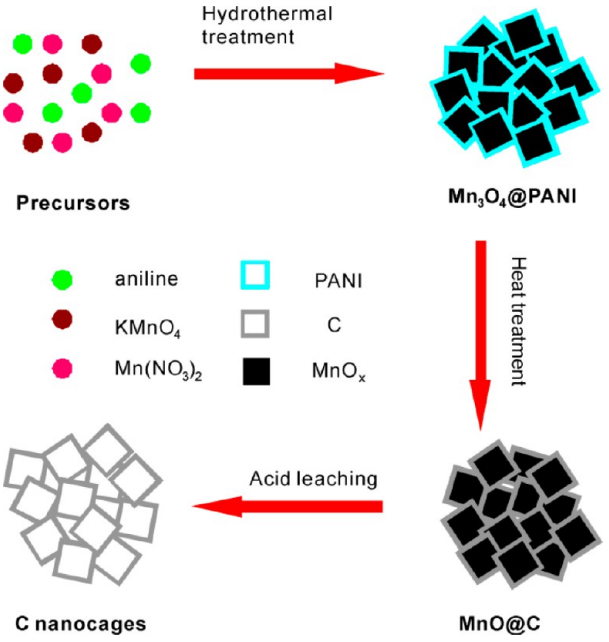

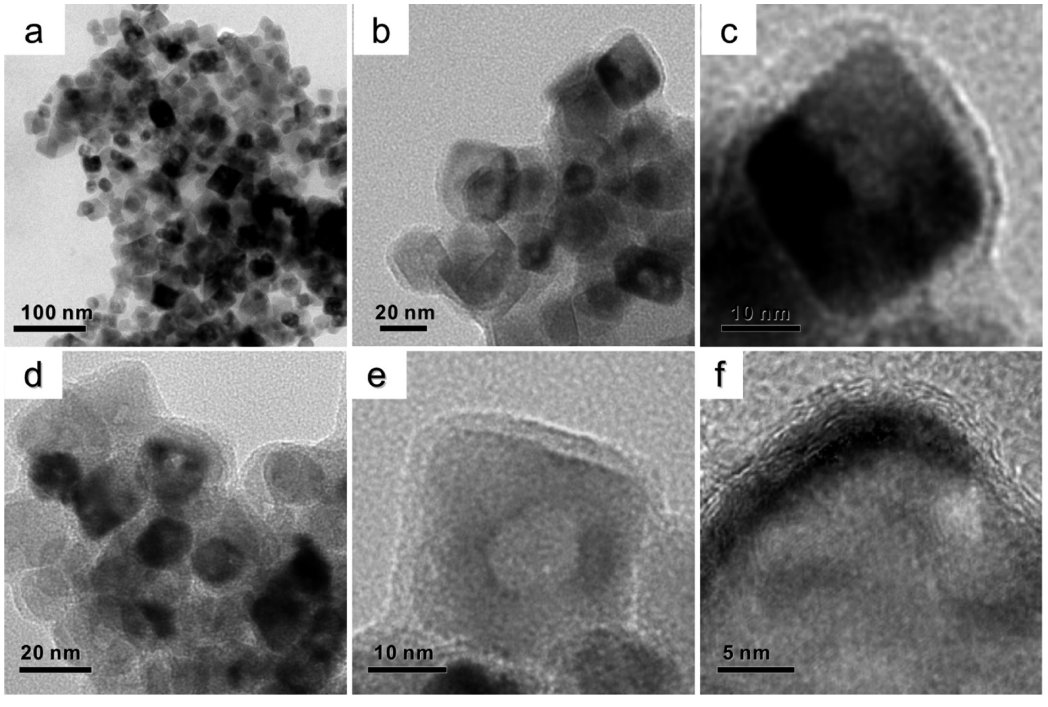

Figure 1. TEM images of Mn_3O_4@PANI (a–c) and MnO@C (d–f) core–shell nanoparticles at different magnifications. The MnO@C nanoparticles were prepared at a carbonization temperature of 800 °C.

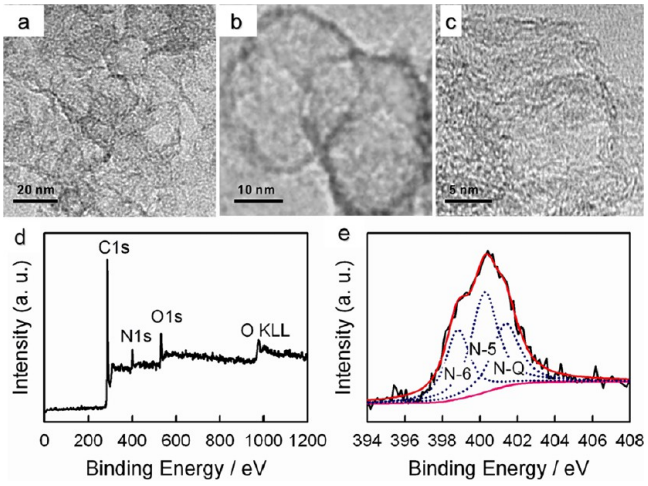

Figure 2. (a–c) TEM images of CNCs-800 at different magnifications. (d) XPS survey spectrum of CNCs-800. (e) High-resolution XPS spectrum of N1s peak.

result (Figure 2c). Energy-dispersive X-ray (EDX) analysis (Figure S2, Supporting Information) reveals that no MnO residue is involved in the CNCs, which is well consistent with the XPS results (Figure 2d). MnO cores were removed sufficiently, and pure CNCs were obtained after acid etching, so the feasible diffusion of electrolyte ions into the CNCs is expected in supercapacitor application. Thermogravimetric analysis (TGA) result (Figure S3, Supporting Information) indicates ca. 5 wt % residual weight, due to the formation of highly stable ceramic materials (e.g., carbon nitrides) at high temperatures.[54] The involvement of N in the CNCs was verified by XPS, which reveals that the weight ratio between C and N in the CNCs is ~11:1 (Figure 2d). High-resolution XPS spectrum of N1s peak is shown in Figure 2e and fitted by three component peaks, namely, pyrrolic/pyridone N (N-5, 400.2 eV), pyridinic N (N-6, 398.7 eV) bonded to two C atoms in six-membered rings at the edge of graphene layer, and quaternary N (N-Q, 401.2 eV) bonded to three C atoms in central or valley position of graphene layer. The locations of nitrogen functionalities within the carbon matrix are schematically displayed in Figure S4, Supporting Information. The peak deconvolution analysis shows that the percentages of N-5, N-6, and N-Q in the CNCs are 41%, 29%, and 30%, respectively. As reported previously, the involvement of nitrogen in the CNCs-800 can improve the wettability of CNCs in the electrolyte and thus enhance the mass-transfer efficiency.[49−54] In addition, the presence of the N-Q within graphene layers can enhance the conductivity of carbon materials.[53,54] Moreover, the presence of N-5 and N-6 can lead to great pseudocapacitance effect and thus increase the capacitance performance.[52,53] It is worth noting that the etching solution after Mn oxide removal (namely, $MnNO_3$ aqueous solution) can be reused for hydrothermal synthesis of Mn_3O_4@PANI nanoparticles, so only carbon source aniline and its oxidant $KMnO_4$ are consumed in the synthesis cycles of CNCs. Thus, we have developed a simple, economical, and efficient approach to preparing ultrathin N-doped graphitic CNCs.

Other carbonization temperatures (700 and 900 °C) were also adopted for heat treatment of Mn_3O_4@PANI nanoparticles. As shown in Figure 3, CNCs-700 and CNCs-900 show morphologies similar to CNCs-800. However, CNCs prepared at different carbonization temperatures have different

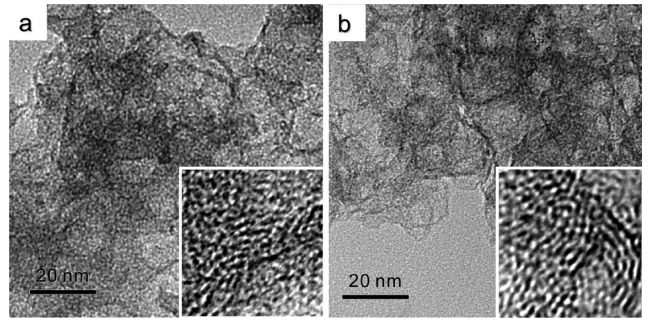

Figure 3. TEM and HRTEM (inset) images of CNCs-700 (a) and CNCs-900.

crystallization degrees. As shown in Figure 4a, the intensity of the diffraction peak at 26.0° increases, while the full width at

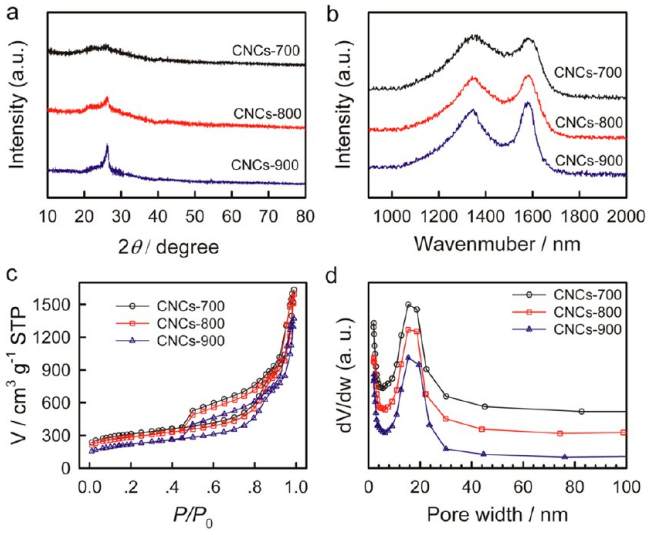

Figure 4. XRD patterns (a), Raman spectra (b), nitrogen adsorption/desorption isotherms (c), and pore size distribution curves (d) of CNCs-700, CNCs-800, and CNCs-900.

half maximum decreases with the increase of carbonization temperature, indicating higher graphitization degree of CNCs at higher temperature. Figure 4b shows the Raman spectra of CNCs prepared at different carbonization temperatures. Two peaks at 1580 and 1345 cm^{-1} could be observed in the Raman spectra of all the CNCs. The peak at 1580 cm^{-1} (G-band) is attributed to the vibration of sp2 hybridized carbon atoms in a 2D hexagonal lattice, while the peak at 1345 cm^{-1} (D-band) is associated with the vibrations of carbon atoms with dangling bonds in plane terminations of the disordered graphite from the defects and disorders of structures in carbon materials.[62] The intensity ratio of D-band to G-band (I_D/I_G) depends on the type of graphitic materials and reflects the graphitization degree. The values of I_D/I_G for CNCs-700, CNCs-800, and CNCs-900 are 0.91, 0.78, and 0.63, respectively, so the graphitic degree of the carbon materials decreases in the order of CNCs-900 > CNC800 > CNCs-700, which is well consistent with XRD results. The TGA data shows that the decomposition temperature increases slightly in the order of CNCs-700 < CNC800 < CNCs-900, also reflecting better crystallization at higher carbonization temperature (Figure S3, Supporting Information).

The specific surface areas of the CNCs prepared at different carbonization temperatures were measured with N_2 adsorption/desorption analysis. Figure 4c shows the adsorption/desorption isotherms of CNCs-700, CNCs-800, and CNCs-900, and the main parameters of all the CNCs are listed in Table S1, Supporting Information. The Brunauer-Emmett-Teller (BET) surface areas of CNCs-700, CNCs-800, and CNCs-900 are 1088, 1001, and 769 $m^2\ g^{-1}$, respectively. The *t*-Plot micropore areas decrease from 471 (CNCs-700) to 394 (CNCs-800) or 219 $m^2\ g^{-1}$ (CNCs-900). From the above results, we can conclude that the decrease of specific surface areas of CNCs at high temperature is mainly ascribed to the decrease of micropore areas, resulting from the higher crystalline degree of the carbon shells. A distinct hysteresis loop can be observed in the larger range of ca. 0.45-1.0 P/P_0, indicating the presence of a mesoporous structure for all CNCs. As shown in Figure 4d, the pore size distributions of all samples are calculated to be ~14 nm on average from desorption data using the Barrett-Joyner-Halenda (BJH) model, well consistent with the TEM results. Due to the good mesoporosity, the total pore volumes of all samples are extremely large. The *t*-Plot micropore volumes decrease gradually from 0.22 (CNCs-700) to 0.18 (CNCs-800) or 0.1 $cm^3\ g^{-1}$ (CNCs-900). Thus, the CNCs prepared at different carbonization temperatures have similar mesoporosity but distinct microporous structures.

Performance of CNCs as electrode materials for supercapacitors was estimated by a symmetrical two-electrode configuration in 6 M KOH aqueous solution (see Experimental Section for details). Figure 5a shows typical cylic voltammo-

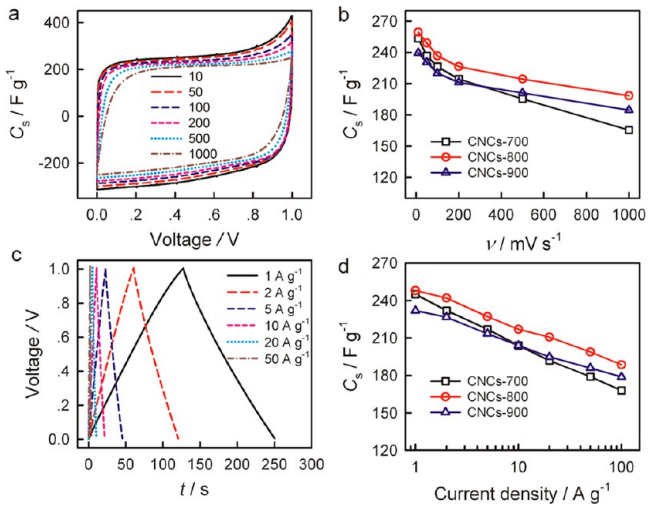

Figure 5. (a) Cyclic voltammograms of CNCs-800 in 6 M KOH aqueous solution at different scan rates. (b) Specific capacitances of CNCs-700, CNCs-800, and CNCs-900 at different scan rates. (c) Galvanostatic charge−discharge curves of CNCs-800 at different current densities (normalized to mass of the active material on a single electrode). (d) Specific capacitance of CNCs-700, CNCs-800, and CNCs-900 at different current densities.

grams of CNCs-800 at different scan rates. Cylic voltammograms of CNCs-800 retain a relatively rectangular shape without a very oblique angle even at a scan rate as high as 1000 mV s^{-1}, indicating the highly capacitive nature with rapid charging−discharging characteristics. The correlation of the specific capacitances for CNCs-700, CNCs-800, and CNCs-900 with the scan rate are shown in Figure 5b. At a given scan rate of 10 mV s^{-1}, the specific capacitances for CNCs-700, CNCs-800, and CNCs-900 are 253, 259, and 240 F g^{-1}, respectively. CNCs-700 and CNCs-800 show comparable specific capacitance values at the low scan rate of 10 mV s^{-1}, but the specific capacitance of CNCs-700 decreases more sharply with increasing the scan rate than that of CNCs-800, probably due to the relatively low conductivity arising of CNCs-700 from poor crystallization at low carbonization temperature. The specific capacitances of CNCs-800 are higher than that of CNCs-900, which is ascribed to the much larger specific surface area of CNCs-800. It is noted that, even at high scan rates of 500 and 1000 mV s^{-1}, the CNCs-800 retain the high specific capacitances of 215 and 198 F g^{-1}, respectively, suggesting that a high specific capacitance can still be maintained under very high power operation.

Galvanostatic charge−discharge measurements for CNC-based symmetrical supercapacitors were also carried out at different current densities. Figure 5c shows typical charge−discharge curves of CNCs-800 at different current densities. The discharge curves of CNCs-800 are highly symmetrical to their corresponding charge counterparts, indicating high charge−discharge efficiency (nearly 100%). Specific capacitances for all CNCs samples at different current densities are presented in Figure 5d. Well consistent with the cyclic voltammetry measurements, CNCs-800 possess specific capacitance higher than CNCs-700 and CNCs-900 at current densities from 1 to 100 A g^{-1}. The specific capacitances of CNCs-700, CNCs-800, and CNCs-900 calculated from discharge curves at a current density of 1 A g^{-1} are 245, 248, and 232 F g^{-1}, respectively. Parallel experiments (three CNCs-800 supercapacitors fabricated similarly) reveal that the deviation of specific capacitance is within 3 F g^{-1}, indicating a high reproducibility. The specific capacitance of CNCs-800 is higher than that of a similar CNC material synthesized by MgO template method with benzene precursor (216 F g^{-1} at 1 A g^{-1} in 6 M KOH electrolyte),[13] highlighting the superior capacitance property of our ultrathin nitrogen-doped graphitic CNCs. The superior specific capacitance of CNCs-800 can be ascribed to the involvement of nitrogen in our CNCs, which can not only improve the wettability of carbon material in the electrolyte but also enhance the conductivity of carbon material.[49−54] Moreover, as listed in Table S2, Supporting Information, the specific capacitance of CNCs-800 is also higher than that of nitrogen-doped carbon materials reported previously, such as N-enriched nanocarbons, N-doped porous nanofibers, and N-enriched CNTs,[49,55−60] highlighting the advantage of the unique ultrathin graphitic cage-like structure. The specific capacitances of all CNCs samples progressively decrease with the increase of the current density from 1 to 100 A g^{-1}, which is correlated with the increasing diffusion limitation. However, the specific capacitances of CNCs-800 at 10 and 100 A g^{-1} still retain high values of 217 and 189 F g^{-1} respectively, which are 88% and 76% of the value at 1 A g^{-1}. From the above discussion, it can be seen that CNCs-800 can show both high specific capacitance and excellent rate capability.

The excellent capacitance properties of CNCs-800 can be ascribed to the combination effect of regular structure, moderate graphitization, large specific surface area, good mesoporosity, and appropriate N doping. These unique structure characteristics can possess several major advantages as follows. (1) The ultrathin carbon shells (~2 nm) with abundant micropores can ensure high specific surface area, which is beneficial for achieving high specific capacitance; (2)

the ultrathin carbon shells can be fully exposed to electrolyte, resulting in little useless surface areas; (3) interconnected micropores and mesopores in CNCs-800 facilitate fast ion transport, ensuring the high rate capability;[63] (4) stacked graphitic carbon shells can ensure fast electron transfer; and (5) appropriate nitrogen doping can further improve the capacitance property.[49−60]

The fast ion diffusion for CNCs-800-based supercapacitor is further confirmed by the Nyquist plot. As shown in Figure 6a,

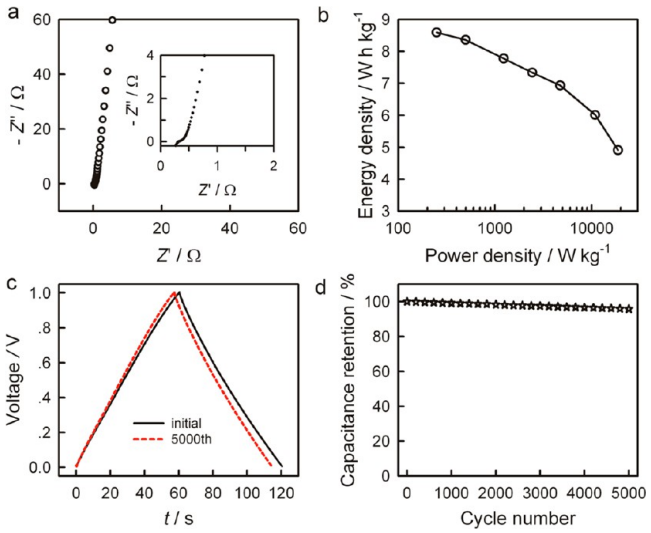

Figure 6. (a) Nyquist plot of CNCs-800-based supercapacitor performed in 6 M KOH aqueous solution. Inset shows the enlarged high-frequency region. (b) Ragone plot of CNCs-800-based supercapacitor. (c) The charge−discharge curves of CNCs-800 before and after 5000 cycles at 2 A g^{-1}. (d) Capacitance retention versus the cycle number measured at 2 A g^{-1}.

the Nyquist plot shows a short Warburg-type line (the slope of the 45° portion of the curve), suggesting fast ion diffusion in the CNCs-800-based electrodes. The low-frequency segment of the impedance spectrum was nearly vertical, indicating a nearly ideal capacitor behavior. The equivalent series resistance (ESR) of CNCs-800 corresponding to the high frequency intercept at the real axis,[3] is estimated to be 0.31 Ω, which is larger than that of CNCs-900 and smaller than that of CNCs-700 (Figure S5, Supporting Information). The power density and energy density are caculated using the charge−discharge data. Figure 6b shows the Ragone plot for CNCs-800-based supercapacitor. The specific energy density is as high as 8.6 Wh kg^{-1} at a current density of 1 A g^{-1}. More importantly, the specific energy densities are still 6.0 and 4.9 Wh kg^{-1} with high specfic power densities of 10.9 and 18.8 kW kg^{-1} at high current densities of 50 and 100 A g^{-1}, respectively. These results indicate that the CNCs-800-based supercapacitor can operate with high power density and high energy density at high rates. The stability of CNCs-800-based supercapacitor was evaluated by examination of 5000 cycles at a galvanostatic charge−discharge current density of 2 A g^{-1}. As shown in Figure 6c,d, the CNCs-800-based supercapacitor still retained ∼95% of its initial capacitance after 5000 cycles, indicating its excellent cycling stability.

The pseudocapacitance behavior of CNCs-800 in 0.5 M H_2SO_4 aqueous solution was investigated using a three-electrode mode. As shown in Figure 7a, all the cyclic voltammograms show wide reversible humps, indicating large

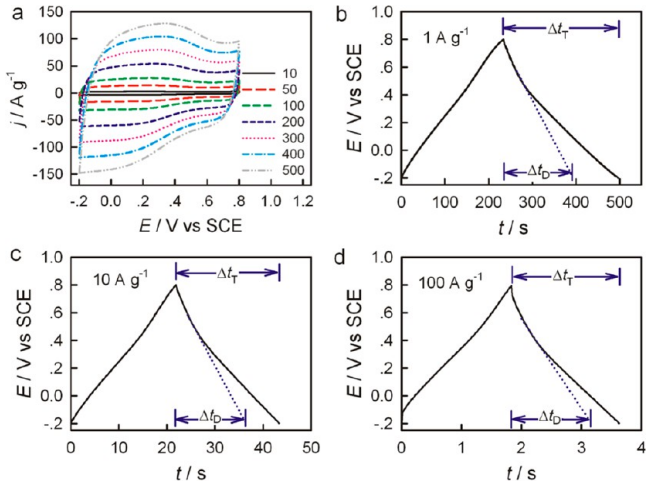

Figure 7. (a) Cyclic voltammograms of CNCs-800 at different scan rates in 0.5 M H_2SO_4 aqueous solution. (b,c) Charge−discharge curves of CNCs-800 at current densities of 1, 10, and 100 A g^{-1}. Δt_D is the discharge time of the double-layer capacitance type, and Δt_T is the total discharge time of the overall capacitance.

faradaic contribution to the overall capacitance performance. For comparison, the electrochemical behavior of a commercial activated carbon without nitrogen doping was examined in 0.5 M H_2SO_4 aqueous solution. As shown in Figure S6, Supporting Information, the commercial activated carbon shows no obvious redox peaks, so we can conclude that the great pseudocapacitance of CNCs-800 is related to the functional nitrogen groups (N-5 and N-6) in CNCs.[53,54] Galvanostatic charge−discharge measurements for CNCs-800 were also carried out at different current densities to better quantify the pseudocapacitance contribution. As shown in Figure 7b,c, all the discharge curves show inflections to a different extent at ∼0.4 V, indicating that the overall capacitance is a mixture of pseudocapacitance and electrochemical double-layer capacitance. The specific capacitance of CNCs-800 in 0.5 M H_2SO_4 aqueous solution calculated from discharge curves at a current density of 1 A g^{-1} is 262 F g^{-1}, which is a little larger than that in 6 M KOH aqueous solution (248 F g^{-1}) due to the presence of great pseudocapacitance in 0.5 M H_2SO_4 aqueous solution. To calculate the pseudocapacitance, extended lines of the linear parts of the discharge curves have been drawn, which represent the double-layer capacitance parts of the discharge curves. Obviously, Δt_D represents the discharge time of the double-layer capacitance type, and Δt_T is the total discharge time of the overall capacitance. Thus, the percentages of pseudocapacitance of CNCs-800 at current density of 1, 10, and 100 A g^{-1} can be calculated roughly to be 39.0%, 33.1%, and 22.4%, respectively, indicating that the percentage of pseudocapacitance decreases with the increase of current density. Because of the decreased pseudocapacitance contribution to the overall capacitance in 0.5 M H_2SO_4 aqueous solution at high current densities, CNCs-800 show almost comparable specific capacitances in alkaline and acidic electrolyte solutions at high current densities from 10 to 100 A g^{-1}. The percentages of pseudocapacitance of CNCs-700 and CNCs-900 at a current density of 1 A g^{-1} are also measured and calculated roughly to be 42.9% and 34.7%, respectively (Figure S7, Supporting Information). The percentage of pseudocapacitance decreases with the increase of carbonization temperature, which is ascribed to different percentages of N components in the CNCs at different

carbonization temperatures. As reported previously, N-5 and N-6 can be converted to N-Q at high temperature, so the presence of less N-5 and N-6 in the CNCs at higher temperatures leads to less pseudocapacitance.[52,53]

4. CONCLUSIONS

In summary, novel ultrathin nitrogen-doped graphitic CNCs derived from PANI were prepared with a simple template method. Manganese oxides play very important roles in the synthesis of CNCs, including serving as template for carbon coating and catalyst for graphitization of carbon shells. Both the surface area and the crystallization degree can be easily tailored by controlling the carbonization temperature. Due to the combination effect of regular structure, moderate graphitization, large specific surface area, good mesoporosity, and appropriate N doping, the CNCs prepared at the optimized temperature of 800 °C show high specific capacitance, outstanding rate capability, and excellent cycling stability in 6 M KOH aqueous solution. The CNCs-800-based supercapacitor can operate with high power density and high energy density at high rates. In addition, the CNCs-800 material exhibits great pseudocapacitance in 0.5 M H_2SO_4 aqueous solution. The ultrathin nitrogen-doped graphitic CNCs is a promising electrode material for an ultrafast and high capacitance energy storage device.

■ ASSOCIATED CONTENT

Supporting Information

Additional figures. This material is available free of charge via the Internet at http://pubs.acs.org.

■ AUTHOR INFORMATION

Corresponding Author

*E-mail: xieqj@hunnu.edu.cn (Q.X.); nfzheng@xmu.edu.cn (N.Z.).

Notes

The authors declare no competing financial interest.

■ ACKNOWLEDGMENTS

This work is supported by the MOST of China (2011CB932403), National Natural Science Foundation of China (21075036, 21175042, 21131005, 20925103), Program for Science and Technology Innovative Research Team in Higher Educational Institutions of Hunan Province, and Start-Up Fund for Young Teachers in Hunan Normal University.

■ REFERENCES

(1) Winter, M.; Brodd, R. J. *Chem. Rev.* **2004**, *104*, 4245.
(2) Simon, P.; Gogotsi, Y. *Nat. Mater.* **2008**, *7*, 845.
(3) Stoller, M. D.; Ruoff, R. S. *Energy Environ. Sci.* **2010**, *3*, 1294.
(4) Bae, J.; Song, M. K.; Park, Y. J.; Kim, J. M.; Liu, M.; Wang, Z. L. *Angew. Chem., Int. Ed.* **2011**, *50*, 1683.
(5) Jiang, H.; Yang, L.; Li, C.; Yan, C.; Lee, P. S.; Ma, J. *Energy Environ. Sci.* **2011**, *4*, 1813.
(6) Qu, Q.; Yang, S.; Feng, X. *Adv. Mater.* **2011**, *23*, 5574.
(7) Miller, J. R.; Simon, P. *Science* **2008**, *321*, 651.
(8) Miller, J. R.; Outlaw, R. A.; Holloway, B. C. *Science* **2010**, *329*, 1637.
(9) Hall, P. J.; Mirzaeian, M.; Fletcher, S. I.; Sillars, F. B.; Rennie, A. J. R.; Shitta-Bey, G. O.; Wilson, G.; Cruden, A.; Carter, R. *Energy Environ. Sci.* **2010**, *3*, 1238.
(10) Zhang, L. L.; Zhao, X. S. *Chem. Soc. Rev.* **2009**, *38*, 2520.
(11) Zhai, Y.; Dou, Y.; Zhao, D.; Fulvio, P. F.; Mayes, R. T.; Dai, S. *Adv. Mater.* **2011**, *23*, 4828.
(12) Dai, L.; Chang, D. W.; Baek, J. B.; Lu, W. *Small* **2012**, *8*, 1130.
(13) Xie, K.; Qin, X.; Wang, X.; Wang, Y.; Tao, H.; Wu, Q.; Yang, L.; Hu, Z. *Adv. Mater.* **2012**, *24*, 347.
(14) Hu, C. C.; Chang, K. H.; Lin, M. C.; Wu, Y. T. *Nano Lett.* **2006**, *6*, 2690.
(15) Wu, Z. S.; Wang, D. W.; Ren, W.; Zhao, J.; Zhou, G.; Li, F.; Cheng, H. M. *Adv. Funct. Mater.* **2010**, *20*, 3595.
(16) Chen, S.; Zhu, J.; Wu, X.; Han, Q.; Wang, X. *ACS Nano* **2010**, *4*, 2822.
(17) Wu, Z. S.; Ren, W.; Wang, D. W.; Li, F.; Liu, B.; Cheng, H. M. *ACS Nano* **2010**, *4*, 5835.
(18) Yu, G.; Hu, L.; Liu, N.; Wang, H.; Vosgueritchian, M.; Yang, Y.; Cui, Y.; Bao, Z. *Nano Lett.* **2011**, *11*, 4438.
(19) Fan, Z.; Yan, J.; Wei, T.; Zhi, L.; Ning, G.; Li, T.; Wei, F. *Adv. Funct. Mater.* **2011**, *21*, 2366.
(20) Yuan, C.; Yang, L.; Hou, L.; Shen, L.; Zhang, X.; Lou, X. W. *Energy Environ. Sci.* **2012**, *5*, 7883.
(21) Yan, J.; Fan, Z.; Sun, W.; Ning, G.; Wei, T.; Zhang, Q.; Zhang, R.; Zhi, L.; Wei, F. *Adv. Funct. Mater.* **2012**, *22*, 2632.
(22) Wang, K.; Huang, J. Y.; Wei, Z. X. *J. Phys. Chem. C* **2010**, *114*, 8062.
(23) Xue, M.; Li, F.; Zhu, J.; Song, H.; Zhang, M.; Cao, T. *Adv. Funct. Mater.* **2012**, *22*, 1284.
(24) Huang, F.; Chen, D. *Energy Environ. Sci.* **2012**, *5*, 5833.
(25) Shi, H. *Electrochim. Acta* **1995**, *41*, 1633.
(26) Qu, D.; Shi, H. *J. Power Sources* **1998**, *74*, 99.
(27) Frackowiak, E.; Béguin, F. *Carbon* **2001**, *39*, 937.
(28) Xu, B.; Wu, F.; Chen, R. J.; Cao, G. P.; Chen, S.; Zhou, Z. M.; Yang, Y. S. *Electrochem. Commun.* **2008**, *10*, 795.
(29) Ruiz, V.; Blanco, C.; Santamaria, R.; Ramos-Fernandez, J. M.; Martinez-Escandell, M.; Sepulveda-Escribano, A.; Rodriguez-Reinoso, F. *Carbon* **2009**, *47*, 195.
(30) Balathanigaimani, M. S.; Shim, W. G.; Lee, M. J.; Kim, C.; Lee, J. W.; Moon, H. *Electrochem. Commun.* **2008**, *10*, 868.
(31) Lota, G.; Fic, K.; Frackowiak, E. *Energy Environ. Sci.* **2011**, *4*, 1592.
(32) Liu, H. Y.; Wang, K. P.; Teng, H. *Cabon* **2005**, *43*, 559.
(33) Ye, J. S.; Liu, X.; Cui, H. F.; Zhang, W. D.; Sheu, F. S.; Lim, T. M. *Electrochem. Commun.* **2005**, *7*, 249.
(34) Wang, L.; Lin, S.; Lin, K.; Yin, C.; Liang, D.; Di, Y.; Fan, P.; Jiang, D.; Xiao, F. S. *Microporous Mesoporous Mater.* **2005**, *85*, 136.
(35) An, K. H.; Kim, W. S.; Park, Y. S.; Moon, J. M.; Bae, D. J.; Lim, S. C.; Lee, Y. S.; Lee, Y. H. *Adv. Funct. Mater.* **2001**, *11*, 387.
(36) Yang, C. M.; Kim, Y. J.; Endo, M.; Kanoh, H.; Yudasaka, M.; Iijima, S.; Kaneko, K. *J. Am. Chem. Soc.* **2006**, *129*, 20.
(37) Hu, L. B.; Choi, J. W.; Yang, Y.; Jeong, S.; Mantia, F. L.; Cui, L. F.; Cui, Y. *Proc. Natl. Acad. Soc. U.S.A.* **2009**, *106*, 21490.
(38) Liu, C.; Yu, Z.; Neff, D.; Zhamu, A.; Jang, B. Z. *Nano Lett.* **2010**, *10*, 4863.
(39) Sun, Y.; Wu, Q.; Shi, G. *Energy Environ. Sci.* **2011**, *4*, 1113.
(40) Huang, Y.; Liang, J.; Chen, Y. *Small* **2012**, *8*, 1805.
(41) Zhu, Y. W.; Murali, S.; Stoller, M. D.; Ganesh, K. J.; Cai, W. W.; Ferreira, P. J.; Pirkle, A.; Wallace, R. M.; Cychosz, K. A.; Thommes, M.; Su, D.; Stach, E. A.; Ruoff, R. S. *Science* **2011**, *332*, 1537.
(42) An, X. H.; Simmons, T.; Shah, R.; Wolfe, C.; Lewis, K. M.; Washington, M.; Nayak, S. K.; Talapatra, S.; Kar, S. *Nano Lett.* **2010**, *10*, 4295.
(43) Shaijumon, M. M.; Ou, F. S.; Ci, L.; Ajayan, P. M. *Chem. Commun.* **2008**, *20*, 2373.
(44) Yang, X.; Zhu, J.; Qiu, L.; Li, D. *Adv. Mater.* **2011**, *23*, 2833.
(45) Wang, X.; Zhi, L. J.; Mullen, K. *Nano Lett.* **2008**, *8*, 323.
(46) Stoller, M. D.; Park, S. J.; Zhu, Y. W.; An, J. H.; Ruoff, R. S. *Nano Lett.* **2008**, *8*, 3498.
(47) Guo, C. X.; Li, C. M. *Energy Environ. Sci.* **2011**, *4*, 4504.
(48) Lei, Z.; Christov, N.; Zhao, X. S. *Energy Environ. Sci.* **2011**, *4*, 1866.
(49) Chen, L. F.; Zhang, X. D.; Liang, H. W.; Kong, M.; Guan, Q. F.; Chen, P.; Wu, Z. Y.; Yu, S. H. *ACS Nano* **2012**, *6*, 7092.
(50) Guo, H.; Gao, Q. *J. Power Sources* **2009**, *186*, 551.

(51) Lee, Y. H.; Lee, Y. F.; Chang, K. H.; Hu, C. C. *Electrochem. Commun.* **2011**, *13*, 50.
(52) Yang, X.; Wu, D.; Chen, X.; Fu, R. *J. Phys. Chem. C* **2010**, *114*, 8581.
(53) Wang, D. W.; Li, F.; Yin, L. C.; Lu, X.; Chen, Z. G.; Gentle, I. R.; Lu, G. Q.; Cheng, H. M. *Chem.—Eur. J.* **2012**, *18*, 5345.
(54) Su, F.; Poh, C. K.; Chen, J. S.; Xu, G.; Wang, D.; Li, Q.; Lin, J.; Lou, X. W. *Energy Environ. Sci.* **2011**, *4*, 717.
(55) Beguin, F.; Szostak, K.; Lota, G.; Frackowiak, E. *Adv. Mater.* **2005**, *17*, 2380.
(56) Hulicova-Jurcakova, D.; Kodama, M.; Shiraishi, S.; Hatori, H.; Zhu, Z. H.; Lu, G. Q. *Adv. Funct. Mater.* **2009**, *19*, 1800.
(57) Lota, G.; Lota, K.; Frackowiak, E. *Electrochem. Commun.* **2007**, *9*, 1828.
(58) Frackowiak, E.; Lota, G.; Machnikowski, J.; Vix-Guterl, C.; Beguin, F. *Electrochim. Acta* **2006**, *51*, 2209.
(59) Jurewicz, K.; Babel, K.; Ziolkowski, A.; Wachowska, H. *J. Phys. Chem. Solids* **2004**, *65*, 269.
(60) Zhong, M.; Kim, E. K.; McGann, J. P.; Chun, S.-E.; Whitacre, J. F.; Jaroniec, M.; Matyjaszewski, K.; Kowalewski, T. *J. Am. Chem. Soc.* **2012**, *134*, 14846.
(61) Tan, Y.; Xu, C.; Chen, G.; Fang, X.; Zheng, N.; Xie, Q. *Adv. Funct. Mater.* **2012**, *22*, 4584.
(62) Wang, Y.; Su, F.; Wood, C. D.; Lee, J. Y.; Zhao, X. S. *Ind. Eng. Chem. Res.* **2008**, *47*, 2294.
(63) Fan, Z.; Liu, Y.; Yan, J.; Ning, G.; Wang, Q.; Wei, T.; Zhi, L.; Wei, F. *Adv. Energy Mater.* **2012**, *2*, 419.